



High efficiency bifacial $\text{Cu}_2\text{ZnSnSe}_4$ thin-film solar cells on transparent conducting oxide glass substrates

Jung-Sik Kim, Jin-Kyu Kang, and Dae-Kue Hwang

Citation: *APL Mater.* **4**, 096101 (2016); doi: 10.1063/1.4962145

View online: <http://dx.doi.org/10.1063/1.4962145>

View Table of Contents: <http://scitation.aip.org/content/aip/journal/aplmater/4/9?ver=pdfcov>

Published by the [AIP Publishing](#)

Articles you may be interested in

[Nanocrystalline \$\text{Cu}_2\text{ZnSnSe}_4\$ thin films for solar cells application: Microdiffraction and structural characterization](#)

J. Appl. Phys. **120**, 051705 (2016); 10.1063/1.4958941

[Detection of \$\text{Cu}_2\text{Zn}_5\text{SnSe}_8\$ and \$\text{Cu}_2\text{Zn}_6\text{SnSe}_9\$ phases in co-evaporated \$\text{Cu}_2\text{ZnSnSe}_4\$ thin-films](#)

Appl. Phys. Lett. **107**, 172102 (2015); 10.1063/1.4934847

[Microstructural analysis of 9.7% efficient \$\text{Cu}_2\text{ZnSnSe}_4\$ thin film solar cells](#)

Appl. Phys. Lett. **105**, 183903 (2014); 10.1063/1.4901401

[Employing time-resolved terahertz spectroscopy to analyze carrier dynamics in thin-film \$\text{Cu}_2\text{ZnSn}\(\text{S,Se}\)_4\$ absorber layers](#)

Appl. Phys. Lett. **104**, 253901 (2014); 10.1063/1.4884817

[Control of an interfacial \$\text{MoSe}_2\$ layer in \$\text{Cu}_2\text{ZnSnSe}_4\$ thin film solar cells: 8.9% power conversion efficiency with a TiN diffusion barrier](#)

Appl. Phys. Lett. **101**, 053903 (2012); 10.1063/1.4740276

NEW Special Topic Sections

NOW ONLINE
Lithium Niobate Properties and Applications:
Reviews of Emerging Trends

AIP Applied Physics Reviews

High efficiency bifacial $\text{Cu}_2\text{ZnSnSe}_4$ thin-film solar cells on transparent conducting oxide glass substrates

Jung-Sik Kim, Jin-Kyu Kang, and Dae-Kue Hwang^a

Convergence Research Center for Solar Energy, Daegu Gyeongbuk Institute of Science and Technology (DGIST), 333 Techno Jungang-daero, Dalsung-gun, Daegu 711-873, South Korea

(Received 2 August 2016; accepted 21 August 2016; published online 1 September 2016)

In this work, transparent conducting oxides (TCOs) have been employed as a back contact instead of Mo on $\text{Cu}_2\text{ZnSnSe}_4$ (CZTSe) thin-film solar cells in order to examine the feasibility of bifacial $\text{Cu}_2\text{ZnSn}(\text{S},\text{Se})_4$ (CZTSSe) solar cells based on a vacuum process. It is found that the interfacial reaction between fluorine doped tin oxide (FTO) or indium tin oxide (ITO) and the CZTSe precursor is at odds with the conventional CZTSe/Mo reaction. While there is no interfacial reaction on CZTSe/FTO, indium in CZTSe/ITO was significantly diffused into the CZTSe layers; consequently, a SnO_2 layer was formed on the ITO substrate. Under bifacial illumination, we achieved a power efficiency of 6.05% and 4.31% for CZTSe/FTO and CZTSe/ITO, respectively. © 2016 Author(s). All article content, except where otherwise noted, is licensed under a Creative Commons Attribution (CC BY) license (<http://creativecommons.org/licenses/by/4.0/>). [<http://dx.doi.org/10.1063/1.4962145>]

$\text{Cu}_2\text{ZnSn}(\text{S},\text{Se})_4$ (CZTSSe) devices have been extensively investigated as promising alternative thin-film photovoltaics (PVs) due to their large absorption coefficient (10^4 cm^{-1}), tunable bandgap (1.0–1.5 eV), and earth-abundance.^{1,2} To date, CZTSSe thin-film solar cells with 10%–12.6% conversion efficiency have been realized.^{3–5} However, the conversion efficiency of CZTSSe thin-film solar cells is still too low to replace commercial CuInGaSe_2 (CIGS) thin-film solar cells (21.6%).⁶ Since conventional CZTSSe devices employ a Mo back contact that reflects light from the rear side, devices can only be illuminated from the front side. One way to increase conversion efficiency is to utilize a bifacial cell design that replaces the Mo contact with a transparent conductive oxide (TCO) layer, which would allow simultaneous illumination from both the front and back sides of the device. A bifacial thin-film photovoltaic using CIGS on TCO was first investigated by Nakada *et al.*,⁷ and the concept was later applied to CIGS and CZTSSe solar cells.^{8–13} Another added benefit of the bifacial design is the ability to utilize these semi-transparent thin-film solar cells in other devices such as tandem solar cells and solar windows.¹⁴ Accordingly, bifacial CZTSSe solar cells using TCO back contacts such as indium tin oxide (ITO), aluminum-doped zinc oxide (AZO), and fluorine-doped tin oxide (FTO) have been studied by many research groups.^{10–13} To date, most reports regarding bifacial CZTSSe were based on solution processing methods. For example, Ge *et al.* reported $\text{Cu}_2\text{ZnSnS}_4$ (CZTS) solar cells prepared through co-electroplating on an ITO substrate, which exhibited only 3.4% conversion efficiency under bifacial illumination.¹⁰ Another report by Ge *et al.* showed that annealing temperatures greater than 500 °C caused In diffusion from the ITO substrate into the CZTSSe layer, resulting in a new CZTISse absorber layer and a SnO_2 inter-layer.¹¹ Mali *et al.* also demonstrated CZTS solar cells with 1.85% efficiency using the successive ionic layer adsorption and reaction (SILAR) method.¹² In general, solution processing for bifacial CZTSSe devices led to lower efficiencies and was ultimately less suitable for industrial production. Alternatively, sputtering is a commonly used preparation technique in the semiconductor industry for low-cost and large-scale production. In order to examine the economic feasibility of bifacial CZTSSe solar cells, studies based on a vacuum-based fabrication process are necessary.

^aElectronic mail: dkhwang@dgist.ac.kr



In this work, CZTSe thin-film solar cells were fabricated on FTO and ITO substrates through a vacuum process using direct current (DC) sputtering. A metallic stack precursor of Cu/Sn/Zn was deposited on FTO- and ITO-coated glass in a DC-magnetron sputter system from 99.99% pure Cu, Sn, and Zn targets at room temperature. The FTO (650 nm) and ITO (150 nm) substrates were chosen on the basis of their sheet resistance ($20 \Omega/\square$). The respective metallic layers were deposited under sputtering powers of 150, 300, and 300 W at a working pressure of 3 mTorr. Metal precursors with a stacking order of Cu (95 nm)/Sn (150 nm)/Zn (105 nm) on the TCO substrate were annealed in a quartz tube furnace with a Se pellet. Based on the current-voltage characteristics of CZTSe solar cells with different absorber thickness (Fig. S1 and Table S1 in the [supplementary material](#)), a $1 \mu\text{m}$ absorber thickness was determined as optimal in this study. After this, the annealing conditions were optimized and the optimal conditions are followed. A two-step selenization was conducted, wherein the samples were heated from room temperature to 300°C over 25 min and then maintained at 300°C for 17 min; subsequently, they were heated from 300 to 500°C over 25 min and then maintained at 500°C for 18 min. Before annealing, the sealed furnace was evacuated to 10^{-3} Torr to remove moisture and impurities. Ar was then used to fill the furnace until the pressure reached 760 Torr. The CZTSe solar cell devices were fabricated by sequentially depositing a ~ 50 nm CdS buffer layer via chemical bath deposition, a ~ 50 nm intrinsic ZnO layer via sputtering, a ~ 300 nm AZO layer via sputtering, and a $1 \mu\text{m}$ -thick Al collection grid via thermal evaporation on the underlying absorber layer. The film structure and morphology were characterized by field-emission scanning electron microscopy (SEM, Hitachi S-4800), transmission electron microscopy (TEM, Hitachi HF-3300), and powder X-ray diffraction (XRD, PANalytical Empyrean) using $\text{CuK}\alpha$ radiation ($\lambda = 0.15406 \text{ nm}$). Depth profiles of CZTSe layers were collected with Scanning Transmission Electron Microscopy (STEM)–Energy Dispersive Spectroscopy (EDS) line scans. Solar cell device performance was measured using a solar simulator (Newport, 94022A) under a simulated air mass 1.5 global (AM 1.5G) spectrum and $100 \text{ mW}/\text{cm}^2$ (1 sun) illumination. The bifacial current-voltage properties were characterized with a 45° mirror illuminating 1 sun from the front side and 0.3 sun from the rear side of the TCO back contacts.

The morphological features of CZTSe absorbers were investigated by collecting SEM images of metal precursors and the annealed layers. Figs. 1(a) and 1(b) present cross-sectional SEM images of the metal precursors with thicknesses of 350 nm on the FTO and ITO substrates, respectively. Since a Cu–Sn alloy can be easily formed at room temperature due to the diffusion of Cu element during precursor deposition,¹⁵ it is hard to observe each layer of Cu, Sn, and Zn on TCO substrate. Figs. 1(c)–1(f) show top-down view and cross-sectional SEM images of the annealed CZTSe layers on the FTO and ITO substrates. The CZTSe absorber thickness was increased to $1 \mu\text{m}$ due to the large volume expansion during the selenization process (Figs. 1(e) and 1(f)).¹⁶ From the top-down

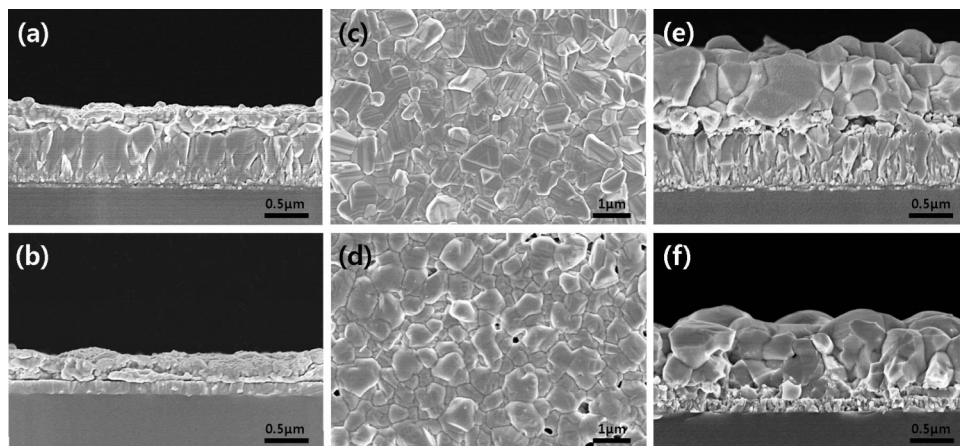


FIG. 1. Cross-sectional SEM images of Cu/Sn/Zn precursor on (a) FTO, and (b) ITO, top-down view SEM images of CZTSe on (c) FTO, and (d) ITO, and cross-sectional SEM images of CZTSe on (e) FTO, and (f) ITO.

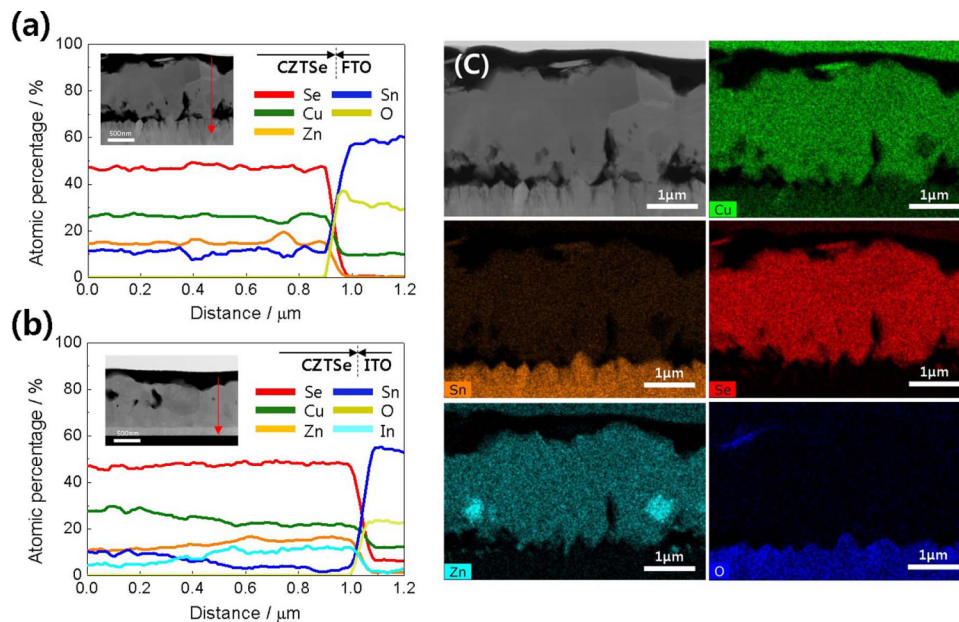


FIG. 2. STEM-EDS line scan profiles of CZTSe on (a) FTO and (b) ITO, and (c) STEM-EDS mapping images of CZTSe on FTO.

image in Fig. 1(c), the CZTSe layer on FTO is uniform and compact. However, Fig. 1(d) indicates that the same layer on ITO shows some voids. The cross-sectional images in Figs. 1(e) and 1(f) indicate that the interfacial adhesion of CZTSe is much better on ITO than on FTO substrates. Compositional analyses of annealed CZTSe absorbers were performed through STEM-EDS measurements. Figs. 2(a) and 2(b) show EDS line scan profiles of CZTSe on FTO and ITO, respectively. The EDS profile of CZTSe on FTO in Fig. 2(a) illustrates that the overall elemental distribution is uniform aside from a Zn-rich zone located near the FTO substrate. The STEM-EDS map in Fig. 2(c) indicates that this zone is likely a Zn-rich secondary phase. Comparatively, the EDS map of the ITO interface in Fig. 2(b) shows that the In intensity increases toward the interface before decreasing significantly on the ITO substrate itself. On the other hand, the Sn intensity is lower at the base of the CZTSe layer and dramatically increases at the ITO substrate. This result demonstrates that Sn atoms diffuse into and substitute In sites into the ITO substrate such that In is segregated from the CZTSe absorber layer. As a result, the In and Sn signals on CZTSe layers and ITO are contrary to expectation. In and Sn diffusion can be explained by the CZTSe formation mechanism. In the case of CZTSe formation from metal precursors, CuSe_x is predominantly formed below 340 °C, and CZTSe is crystallized above 420 °C.¹⁷ Also, because Sn melts at 232 °C, liquid Sn is encountered on the ITO substrate during the first selenization step. Since Sn^{4+} can replace In^{3+} in the ITO substrate,¹⁸ the liquid Sn diffuses into In, and forms the SnO_2 layer. As a result, the segregated In is out-diffused to the absorber layer. This movement probably enhances the interfacial adhesion for CZTSe/ITO, but leads to several voids in the absorber layer. Many studies have also reported void formation in CZTSe due to Sn reaction and movement.¹⁹ The obtained result is in accord with reports from Ge *et al.*,¹¹ which showed that CZTS was converted to CZTIS, and a SnO_2 interlayer between CZTIS and ITO was observed as a result of In diffusion. However, in this work, the ITO was completely converted to SnO_2 . This disparity could be due to the different precursors and annealing conditions. The precursors used by Ge *et al.* were solution-based metal sulfides that were annealed in a Se atmosphere (CZTSSe), whereas pure metal precursors were annealed in a Se atmosphere in this work (CZTSe). Since the reaction mechanism for CZTSSe absorber formation is greatly influenced by the precursor stacking order, deposition method, and S:Se ratio under the annealing conditions, it is unsurprising that the results for SnO_2 formation on the ITO substrate in this study would differ from those of Ge *et al.*

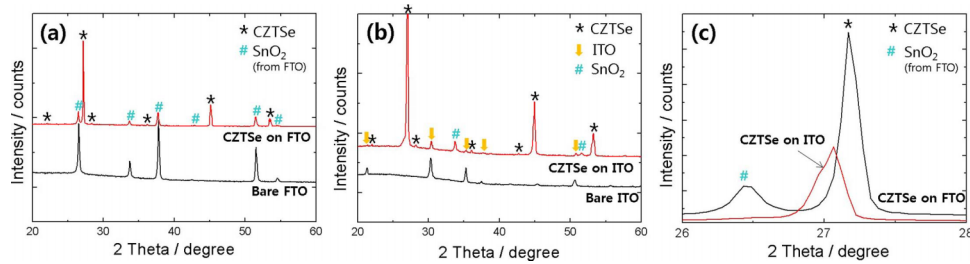


FIG. 3. XRD patterns of CZTSe on (a) FTO and (b) ITO, and (c) magnified CZTSe (112) peak on FTO and ITO.

XRD patterns were collected to determine the crystalline phases of CZTSe films. Fig. 3 shows XRD patterns of annealed CZTSe layers on FTO and ITO. The XRD patterns in Figs. 3(a) and 3(b) confirm that the CZTSe layers on FTO and ITO are in agreement with the tetragonal kesterite phase (PDF 98-009-5117). No secondary Zn-rich phase was identified in the pattern. Only an additional SnO₂ peak from the FTO substrate was observed. One possible explanation for the detection of the Zn-rich secondary phase in TEM and not XRD is the structural similarity between CZTSe and the secondary phase.²⁰ The XRD pattern collected from the CZTSe layer on ITO in Fig. 3(c) shows peaks shifted toward lower angles. This result is in accord with In diffusion out of the ITO substrate and concomitant ionic exchange with Sn in the CZTSe layers, causing lattice expansion.¹⁰ In addition to the main CZTSe peaks, SnO₂ peaks that were not detected on a bare ITO substrate were observed in absorbers on ITO. This observation is consistent with the STEM-EDS result in Fig. 2(b).

Fig. 4 and Table I give the J - V curves and corresponding electrical properties of CZTSe solar cells on FTO and ITO under front, rear, and bifacial illumination. Note that the front, rear, and bifacial light intensities were 1, 0.3, and 1.3 sun, respectively. The conversion efficiency of CZTSe on FTO was 5.72% and 0.51% under front and rear illumination, respectively, which improved to 6.05% under bifacial illumination. This improvement can be primarily attributed to the increase in short circuit current. To date, this accounts for the highest efficiency reported for a CZTSe device with a TCO back contact. Compared with the J_{sc} , the open circuit voltage (V_{oc}) was decreased. This could be a result of a non-Ohmic back contact. Gunawan *et al.*²¹ reported that low V_{oc} values under high illumination intensities can be explained based on three factors: (1) low bulk conductivity, (2) bulk or interface defects, and (3) a non-Ohmic back contact. Since factors (1) and (2) are associated with the V_{oc} pinning behavior, which explains the V_{oc} increase saturation beyond some light intensity, V_{oc} decrease at high light intensity cannot be explained by these factors. In that case, a non-Ohmic back contact that manifests the V_{oc} bending behavior at high light intensity would inhibit an increase in V_{oc} under bifacial illumination. According to the Schottky diode model with one PV

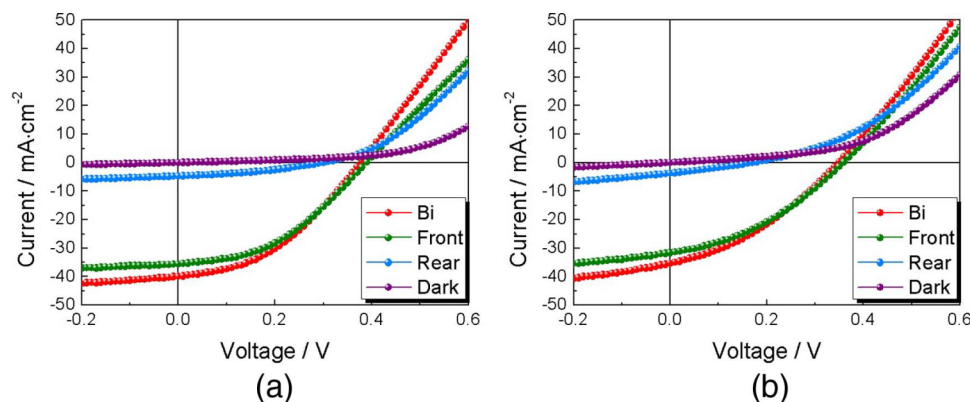


FIG. 4. Current-voltage characteristics of CZTSe solar cells on (a) FTO, and (b) ITO under bifacial, front, rear, and dark illumination.

TABLE I. Summary of device parameters for CZTSe films on FTO and ITO.

| | | η (%) | V_{oc} (V) | J_{sc} (mA/cm ²) | FF (%) | R_s (Ω cm ²) | R_{sh} (Ω cm ²) |
|-----|----------|------------|--------------|--------------------------------|--------|------------------------------------|---------------------------------------|
| FTO | Bifacial | 6.05 | 0.377 | 39.4 | 40.8 | 2.8 | 221.8 |
| | Front | 5.72 | 0.389 | 35.0 | 42.0 | 2.4 | 396.6 |
| | Rear | 0.51 | 0.300 | 4.7 | 36.4 | 7.3 | 935.1 |
| ITO | Bifacial | 4.31 | 0.348 | 35.1 | 35.3 | 2.3 | 163.7 |
| | Front | 4.12 | 0.359 | 31.7 | 36.7 | 2.4 | 201.5 |
| | Rear | 0.57 | 0.170 | 3.7 | 28.7 | 4.0 | 320.1 |

junction and a reverse parasitic back contact,²² if the voltage generated across the Schottky diode is small, V_{oc} can be written as

$$V_{oc} = \frac{kT}{q} \ln \left(\frac{I_{LF}}{I_{FS}} + 1 \right) - (\alpha_F I_{LF} + I_{LR}) R_{BC}, \quad (1)$$

where I_{LF} and I_{LR} are photogenerated currents at the front and rear junctions, I_{FS} is the saturation current at the front junction, α_F is the injection efficiency at the front junction, and R_{BC} is the shunt resistance across the rear junction. If the back contact is not Ohmic, R_{BC} tends to increase with light intensity.²¹ Based on Equation (1), higher R_{BC} under enhanced illumination would increase the negative voltage to the main PV junction with a corresponding decrease in V_{oc} . This is in accord with the observations in Table I. Ge *et al.*¹⁰ also observed a similar decrease in V_{oc} with CZTS films on ITO under bifacial illumination due to a non-Ohmic contact. To enhance the quality of the CZTSe/FTO interface in Fig. 1(c), either additional elements such as ZnO,²³ Ag,²⁴ and carbon²⁵ could be used or rapid thermal annealing²⁶ could be employed.

CZTSe devices on ITO had efficiencies of 4.12% and 0.57% under front and rear illumination, respectively. Similar to FTO-based devices under bifacial illumination, the power efficiency increased to 4.31% due to a corresponding increase in the short circuit current. However, the low V_{oc} phenomenon was also observed, which still suggests a non-Ohmic back contact. In comparison to CZTSe/FTO devices, CZTSe/ITO showed a smaller fill factor. At the same time, CZTSe/ITO devices possessed a smaller shunt resistance (R_{sh}) as shown in Table I. These differences could be due to Sn diffusion into the ITO substrate and exchange with In atoms. Displaced In atoms then diffused back into the absorber layer, which increased the Sn/In ratio in the ITO layer. This in turn caused the formation of SnO₂, which was observed by XRD (Fig. 3(b)) and EDS (Fig. 2(b)). This diffusion reaction could significantly degrade ITO conductivity and may be related to the large voids observed in CZTSe layers. When a moderate amount of Sn ($C_{Sn} \approx 9$ at.%) is doped into In₂O₃, the electrical conductivity is increased due to a larger carrier concentration. However, when Sn is doped beyond 20 at.%, electronic scattering contributes to electrical losses, which outweighs any increases attributed to carrier concentration.¹⁸ From this viewpoint, excessive SnO₂ formation could be the main reason for poor device efficiency. The cross-over behavior between the dark and light J - V curves exhibited by both CZTSe/FTO and CZTSe/ITO in Figs. 4(a) and 4(b) suggests a back contact problem, further supporting a decrease in V_{oc} under bifacial illumination. To minimize the damage and loss of electrical conductivity in ITO, annealing temperatures should be kept below 500 °C.¹¹ At the same time, In and Sn diffusion in CZTSe can be mitigated by implementing a thin barrier layer such as Mo,⁸ ZnO,²³ TiN,²⁷ and TiB₂²⁸ between ITO and the precursor. The optical properties and external quantum efficiency (EQE) curves of CZTSe on FTO and ITO were also measured (Figs. S2 and S3 in the [supplementary material](#)). The optical absorption coefficient α of the absorber layer is $1.2\text{--}2.5 \times 10^4$ cm⁻¹, which is in accord with a previous work.²⁹ The estimated bandgaps from the EQE curves of the CZTSe on FTO and ITO are 0.996 and 0.986 eV, respectively. A more detailed explanation can be found in the [supplementary material](#).

In summary, CZTSe on FTO exhibited 5.72% and 6.05% conversion efficiencies under front and bifacial illumination, respectively. The improved efficiency under bifacial light mainly results from increased current. Yet, compared to front illumination, the V_{oc} decreased due to a non-Ohmic

contact at the CZTSe/TCO interface. In the case of CZTSe on ITO, annealing at high temperatures (500 °C) facilitated In diffusion into CZTSe from the ITO substrate. As a result, SnO₂ formed on ITO, which led to a smaller conversion efficiency of 4.31% under bifacial illumination. In order to suppress In incorporation into CZTSe layers, intermediate layers or milder annealing temperatures are necessary. Although the reaction between CZTSe and the TCO substrate should be controlled, these results still account for the highest reported efficiency for a vacuum-processed CZTSe/TCO device structure to date.

See the [supplementary material](#) for electrical properties of CZTSe solar cells with different absorber thickness, optical properties, and EQE curve of CZTSe absorbers.

This work was supported by the DGIST R&D Programs of the Ministry of Science ICT and Future Planning of Korea (Grant No. 16-BD-05).

- ¹ K. J. Yang, J. H. Sim, D. H. Son, D. W. Kim, G. Y. Kim, W. Jo, S. Song, J. H. Kim, D. Nam, H. Cheong, and J. K. Kang, *Prog. Photovoltaics* **23**, 1771–1784 (2015).
- ² K. J. Yang, D. H. Son, S. J. Sung, J. H. Sim, Y. I. Kim, S. N. Park, D. H. Jeon, J. S. Kim, D. K. Hwang, C. W. Jeon, D. Nam, H. Cheong, J. K. Kang, and D. H. Kim, *J. Mater. Chem. A* **4**, 10151–10158 (2016).
- ³ W. Wang, M. T. Winkler, O. Gunawan, T. Gokmen, T. K. Todorov, Y. Zhu, and D. B. Mitzi, *Adv. Energy Mater.* **4**, 1301465 (2013).
- ⁴ B. Shin, O. Gunawan, Y. Zhu, N. A. Bojarczuk, S. J. Chey, and S. Guha, *Prog. Photovoltaics* **21**, 72–76 (2013).
- ⁵ Y. S. Lee, T. Gershon, O. Gunawan, T. K. Todorov, Y. Virgus, and S. Guha, *Adv. Energy Mater.* **12**, 1401372–1401374 (2015).
- ⁶ P. Jackson, D. Hariskos, R. Wuerz, O. Kiowski, A. Bauer, T. M. Friedlmeier, and M. Powalla, *Phys. Status Solidi RRL* **9**, 28–31 (2014).
- ⁷ T. Nakada, Y. Hirabayashi, and T. Tokado, *Jpn. J. Appl. Phys., Part 2* **41**, L1209–L1211 (2002).
- ⁸ T. Nakada, Y. Hirabayashi, T. Tokado, D. Ohmori, and T. Mise, *Sol. Energy* **77**, 739–747 (2004).
- ⁹ S. H. Moon, S. J. Park, Y. J. Hwang, D. K. Lee, Y. Cho, D. W. Kim, and B. K. Min, *Sci. Rep.* **4**(4408), 1–6 (2014).
- ¹⁰ J. Ge, J. Chu, J. Jiang, Y. Yan, and P. Yang, *ACS Appl. Mater. Interfaces* **6**, 21118–21130 (2014).
- ¹¹ J. Ge, J. Chu, J. Jiang, Y. Yan, and P. Yang, *ACS Sustainable Chem. Eng.* **3**, 3043–3052 (2015).
- ¹² S. S. Mali, B. M. Patil, C. A. Betty, P. N. Bhosale, Y. W. Oh, S. R. Jadhkar, R. S. Devan, Y. R. Ma, and P. S. Patil, *Electrochim. Acta* **66**, 216–221 (2012).
- ¹³ J. Ge, J. Chu, Y. Yan, J. Jiang, and P. Yang, *ACS Appl. Mater. Interfaces* **7**, 10414–10428 (2015).
- ¹⁴ J. H. Yoon, J. Song, and S. J. Lee, *Sol. Energy* **85**, 723–733 (2011).
- ¹⁵ K. N. Tu, *Mater. Chem. Phys.* **46**, 217–223 (1996).
- ¹⁶ L. Guo, Y. Zhu, O. Gunawan, T. Gokmen, V. R. Deline, S. Ahmed, L. T. Romankiw, and H. Deligianni, *Prog. Photovoltaics* **22**, 58–68 (2014).
- ¹⁷ C. M. Fella, A. R. Uhl, C. Hammond, I. Hermans, Y. E. Romanyuk, and A. N. Tiwari, *J. Alloys Compd.* **567**, 102–106 (2013).
- ¹⁸ G. Frank and H. Köstlin, *Appl. Phys. A* **27**, 197–206 (1982).
- ¹⁹ A. Fairbrother, X. Fontané, V. Izquierdo-Roca, M. Placidi, D. Sylla, M. Espindola-Rodriguez, S. López-Mariño, F. A. Pulgarín, O. Vigil-Galán, A. Pérez-Rodríguez, and E. Saucedo, *Prog. Photovoltaics* **22**, 479–487 (2014).
- ²⁰ I. V. Dudchak and L. V. Piskach, *J. Alloys Compd.* **351**, 145–150 (2003).
- ²¹ O. Gunawan, T. Gokmen, and D. B. Mitzi, *J. Appl. Phys.* **116**, 084504 (2014).
- ²² M. Green, A. W. Blakers, J. Zhao, A. M. Milne, A. Wang, and X. Dai, *IEEE Trans. Electron Devices* **37**, 331–336 (1990).
- ²³ S. López-Marino, M. Placidi, A. Pérez-Tomás, J. Llobet, V. Izquierdo-Roca, X. Fontané, A. Fairbrother, M. Espindola-Rodriguez, D. Sylla, A. Pérez-Rodríguez, and E. Saucedo, *J. Mater. Chem.* **1**, 8338–8343 (2013).
- ²⁴ H. Cui, Z. Liu, F. Liu, X. Hao, N. Song, and C. Yan, *Appl. Phys. Lett.* **104**, 041115 (2014).
- ²⁵ F. Zeng, K. Sun, L. Gong, L. Jiang, F. Liu, Y. Lai, and J. Li, *Phys. Status Solidi RRL* **9**(12), 687–691 (2015).
- ²⁶ X. Liu, H. Cui, C. Kong, X. Hao, Y. Huang, F. Liu, N. Song, G. Conibeer, and M. Green, *Appl. Phys. Lett.* **16**, 131110 (2015).
- ²⁷ B. Shin, Y. Zhu, N. A. Bojarczuk, S. J. Chey, and S. Guha, *Appl. Phys. Lett.* **101**, 053903 (2012).
- ²⁸ F. Liu, K. Sun, W. Li, C. Yan, H. Cui, L. Jiang, X. Hao, and M. Green, *Appl. Phys. Lett.* **104**, 051105 (2014).
- ²⁹ Y. Liu, D.-Y. Kong, H. You, C.-L. Chen, X.-H. Lin, and J. Brugger, *J. Mater. Sci. Mater. Electron* **24**, 529–535 (2013).